



Soft Matter

Microstructure of Continuous Shear Thickening Colloidal Suspensions Determined by Rheo-VSANS and Rheo-USANS

| | |
|-------------------------------|--|
| Journal: | <i>Soft Matter</i> |
| Manuscript ID | SM-ART-02-2022-000215.R1 |
| Article Type: | Paper |
| Date Submitted by the Author: | 20-Apr-2022 |
| Complete List of Authors: | Lee, Yu-Fan; University of Delaware, Chemical Engineering Luo, Yimin; University of Delaware, Chemical Engineering Bai, Tainyi; University of Delaware, Chemical Engineering Brown, Scott; Chemours Co, Titanium Technologies Wagner, Norman; University of Delaware, Chemical Engineering |
| | |

SCHOLARONE™
Manuscripts

Microstructure of Continuous Shear Thickening Colloidal Suspensions Determined by Rheo-VSANS and Rheo-USANS

Yu-Fan Lee,^a Yimin Luo,^a Tianyi Bai,^a Scott C. Brown,^b and Norman J. Wagner^a

^a Center for Neutron Science, Department of Chemical and Biomolecular Engineering, University of Delaware, Newark, Delaware 19716

^b The Chemours Company, Chemours Discovery Hub, Newark, Delaware 19713

Abstract

Research on shear thickening colloidal suspensions demonstrates that measurements of the microstructure can elucidate the source of the rheological material properties in the shear thickened state as well as critically test simulations and theory based on a variety of mechanisms such as enhanced lubrication hydrodynamics, elasto-hydrodynamics, and contact friction. Prior work on continuous shear thickening dispersions with a well-defined shear thickened state identified the formation of hydroclusters as characteristic of this state, determined the anisotropy in the nearest neighbor distribution, and used this information to test prevailing theories and simulations. However, important questions remain about the mesoscale (i.e., particle cluster scale) microstructure of the shear thickened state. Here we employ neutron scattering methods applied to shearing colloidal dispersions of spherical particles with two extremes of friction and lubrication surface properties to resolve the longer-length scale microstructure in the shear thickened state. Hydroclusters are shown to be highly localized, in agreement with prior neutron scattering and direct optical measurements, but in disagreement with the most recent simulations that predict a longer-range structure formation. These results combined with prior measurements provide experimental evidence about the length scale of microstructure formation in continuous shear thickening suspensions necessary to improve our understanding of the phenomenon as well as guide theoretical investigations that quantitatively link nanoscale forces to macroscopic properties in the shear thickened state.

1 Introduction

The evolution of the particle-level microstructure of suspensions under flow is of significant scientific interest as it connects the colloidal and microscale forces to the macroscopic rheological behavior of the suspension.^{1, 2} In particular, shear thickening is intimately linked to the microstructure changes that occur when the suspension is forced out of equilibrium during shear. Recent³ and earlier^{1, 4} reviews document the rich history and current research approaches to understand and model shear thickening. Here our focus is on continuous shear thickening suspensions with a well-defined shear thickened state with reproducible material properties.⁵ Several particle-level mechanisms, including lubrication

hydrodynamics,^{4, 6-8} elastohydrodynamics,^{9, 10} and friction contact¹¹⁻¹⁴, have been proposed to model shear thickening in colloidal and non-colloidal suspensions. These models propose particle interactions operating on the nanoscale that affect the bulk rheological behavior of suspensions through both direct contributions to the stresses under flow as well as the microstructure. This research has raised numerous fundamental questions, including the extent of microstructure formation in the shear thickened state. Further, differences in model predictions for the full tensorial form of stress, especially the sign of first normal stress differences N_1 , remains a topic of debate.¹⁵

Despite the complex nature of underlying micromechanical mechanisms of particle interaction, a consensus is emerging that regardless of the nature of the nanoscale interparticle interactions, the formation of *hydroclusters* is a fundamental characteristic of shear thickening. A term coined by Brady and Bossis^{16, 17} and used in a publication by Maranzano and Wagner,¹⁸ *hydroclustering* refers to the reversible particle clustering phenomenon first observed in Stokesian Dynamics simulations.¹⁶ Since the first experimental observations using rheo-optical methods to observe this structuring concurrent with shear thickening by D'Haene et al.¹⁹ and Bender and Wagner,²⁰ a number of other methods, including Rheo-SANS²¹⁻²⁵ (small angle neutron scattering) and rheo-microscopy²⁶ have also confirmed the phenomenon.

Simulation results²⁷ demonstrated that the inclusion of simplified lubrication hydrodynamics along the lines of centers between particles alone sufficed to generate hydroclusters, leading to shear thickening via increased lubrication hydrodynamics, and that the inclusion of nanoscale forces beyond smooth hard sphere interactions between particles further amplifies the viscosity increase in the shear thickened state.^{28, 29} This structuring at high global Péclet number but low particle Reynolds number was presaged by the seminal work of G.K. Batchelor showing the presence of closed streamlines in the two-particle limit as a consequence of lubrication hydrodynamics.^{30, 31} Later solutions of the formally exact Smoluchowski equation for colloidal hard spheres in the dilute limit with full hydrodynamics confirm that hydroclustering leads to a continuous increase in viscosity in the shear thickened state, with well-defined first and second normal stress differences being negative.³²

In addition to extensive investigations by advanced Stokesian Dynamics simulations³³ extending the results to larger systems, others have focused on more complex interactions beyond smooth hard spheres in an attempt to address quantitative discrepancies with experiments.⁵ These include the inclusion of particle-particle contact friction,^{11, 12, 14, 34} elastohydrodynamics,⁹ and enhanced lubrication hydrodynamics.^{7, 8} Extensive comparisons of these simulations and theories against rheological measurements for a wide variety of

colloidal particles with varying nanoscale interparticle interactions, including friction and adsorbed polymers, demonstrate that it is essential to also compare with normal stress differences in addition to the viscosity to distinguish which nanoscale forces are dominant.¹⁵ Additional comparisons of microstructure measurements in the shear thickened state with theory and simulations demonstrated the increase in number of nearest neighbor particles leading to an increase in viscosity, a rich anisotropy of the nearest neighbor distribution, and its connection to the first normal stress difference in the shear thickened state.²⁵

The suspension properties in the shear thickened state are a convolution of the nanoscale forces with the hydroclustered microstructure, but this microstructure is itself dependent upon the same nanoscale forces. This coupling complicates the rigorous testing of simulations with various models for nanoscale interparticle interactions against experimental results. An important observation arising from such comparisons is the need to better understand the extent of cluster formation and its relationship to the amplitude of the shear thickening. The work presented here builds upon earlier studies of the extent of hydroclustering in model colloidal suspensions using Rheo-SANS and Rheo-USANS^{21, 22, 35} as well as direct microscopy under shear²⁶ to compare with the most recent simulation results for enhanced lubrication hydrodynamics⁷ and simulations incorporating contact friction.¹² In addition to presenting new Rheo-USANS results for the angle averaged extent of structuring in the shear thickened state for particles of varying nanoscale interparticle interactions, we also present new measurements of hydrocluster anisotropy in the velocity-vorticity (1-3) plane of flow using advances in Rheo-VSANS (very small angle neutron scattering) metrology. An analysis of the hydrocluster size shows important differences with simulation results.

2 Materials and Methods

2.1 Materials

Suspensions of particles with two different classes of surface properties are studied in this work. Both are based on Stöber particles of a nominal diameter ($2a$) of 370 nm with low polydispersity and synthesized using standard methods.³⁶ One batch was dispersed as is in near-index matching polyethylene glycol to study nominally “bare” silica with the associated level of contact friction.¹⁵ To study particles with a stabilized surface that will have little to no interparticle contact friction, PEGylated silica particles were synthesized by performing silanization of the same batch of Stöber silica through bulk deposition on particles using 2-[methoxy(polyethyleneoxy)6-9]propyltrimethoxysilane from Gelest Inc. The silica to the coupling agent weight ratio was 100:4. Thermogravimetric and carbon analysis confirmed the successful grafting of silica, indicating a grafting density of 3-4 PEG chains/nm². Details of silanization synthesis and thermogravimetric and carbon analysis are documented in the

supplementary materials. Particles were washed and dried properly to remove the excess reactants before suspension formulation.

Concentrated bare and PEGylated silica colloidal suspensions were formulated by dispersing the particles in an index-matched solvent, polyethylene glycol (PEG-200, with an average molecular mass of 200 g/mol, $\eta_m=0.067$ Pa.s at 20 °C), at 63.2 wt%. The mixtures were mechanically stirred to break up large agglomerates using a Tissue-Tearor homogenizer followed by roll mixing for at least one day before rheological measurements.

The volume fraction calculated from the skeletal density of the particles will underestimate the rheological volume fraction due to the porosity of the particles. An effective hard sphere volume fraction, $\phi_{\text{eff},\infty}$, calculated from the measured high-shear plateau viscosity,^{37, 38} is used for the following analysis throughout this work. Dynamic light scattering (DLS) measurements of the hydrodynamic radius yield 197 nm for PEGylated silica and 189 nm for bare silica with finite polydispersity. The number averaged value of particle radius for bare silica is calculated assuming a Schulz distribution, yielding a particle radius of 186 nm. Model prediction using the effective volume fraction and number averaged radius is consistent with our SANS results for both suspensions. A summary of particle and suspension properties is listed in Table I.

Table I: Summary of particle and suspension properties.

| Properties | Symbol Units | Method | Bare Silica | PEGylated Silica |
|--------------------------|--------------------|---------------------------------------|-------------|---------------------|
| Particle radius | a (nm) | DLS [#] | 189 ± 26 | 197 ± 21 |
| | | Calculated number-average value | 186 | |
| Polydispersity | (%) | DLS | 13.9 ± 4.1 | 10.5 ± 5.0 |
| Particle density | d (g/cc) | Densitometry | 2.18 ± 0.02 | 1.98 ± 0.02 |
| Friction coefficients | μ_{fit} | Rheological model | 0.60 | 0.14 |
| Flow-SANS measurement | T (°C) | Thermocouple | 20 | 20 |

| | | | | |
|--|--|-------------------------|-------------------|-------------------|
| temperature | | | | |
| Suspending fluid viscosity | η_m (Pa-s) | Rheometry | 0.067 | 0.067 |
| Suspending fluid density | d_m (g/cc) | Densitometry | 1.126 | 1.126 |
| Weight fraction | wt% | Gravimetric | 63.2 ± 0.1 | 63.2 ± 0.1 |
| Volume fraction | ϕ | Calculated from density | 0.470 ± 0.002 | 0.494 ± 0.003 |
| Relative high-shear viscosity | $\eta_{r,\infty}$ (Pa-s) | Rheometry | 13.5 | 15.5 |
| Effective high-shear viscosity volume fraction | $\phi_{\text{eff},\infty}$ | Rheometry | 0.52 | 0.53 |
| Stress at onset of shear thickening | σ_{onset} (Pa) | Rheometry | 30 | 70 |
| Scattering length density (SLD) of the particle | β_p (10^{-6} \AA^{-2}) | Fitted from USANS | 2.80 | 3.30 |
| Scattering length density (SLD) of the solvent | β_s (10^{-6} \AA^{-2}) | Calculated | 0.517 | 0.517 |
| Scattering length density (SLD) of the organic layer | β_{sh} (10^{-6} \AA^{-2}) | Calculated | - | 0.517 |
| Thickness of the organic layer | t (nm) | Calculated | - | 2.39 |
| Porosity | (%) | Calculated | 22 | 4.0 |

#DLS reports z-averaged diameter, while HS model in SANS reports the number-average diameter. Uncertainty ranges represent one standard deviations reflecting polydispersity of particles.

2.2 Shear rheology measurements

Steady shear rheology was measured both on and off the beamline for bare and PEGylated silica suspensions using stress-controlled rheometers. For the off beamline rheology measurement, an AR-G2 rheometer (TA Instruments, New Castle, DE) with a 40

mm 1° cone and plate geometry was used to measure the viscosity and first normal stress difference, N_1 , where inertial correction is considered using the standard correction procedure.⁵ A preshear protocol at 2000 Pa for at least 30 mins was applied to remove any effects of sample loading and to break up any remaining aggregates in the sample. A conditioning protocol was then applied with forward and backward ramps from 1 to 1000 Pa. At least two cycles of conditioning protocols were performed before the actual flow sweep measurements. The stress flow sweep was then performed after the preshear and conditioning steps, where reversible flow curves with negligible hysteresis were observed for all samples. For the rheology measurements performed in-situ in Rheo-VSANS and Rheo-USANS, Anton Paar rheometers MCR-501 and MCR-301, respectively, were used with a special Couette cell adapted for simultaneous neutron scattering measurements as described in the following. Similar preshear protocols were applied before any measurement on the neutron beamline.

2.3 Rheo-USANS measurements

The small angle neutron scattering experiments were performed at the NIST Center for Neutron Research in Gaithersburg, MD, USA. Ultra-small angle neutron scattering (USANS) measurements were performed on the BT5 instrument with a q -range from $5 \times 10^{-5} \text{ \AA}^{-1}$ to $1.5 \times 10^{-3} \text{ \AA}^{-1}$, where $q = 4\pi \times \sin(\theta/2)/\lambda$ with the neutron wavelength $\lambda = 2.4 \text{ \AA}$ and the wavelength spread $\Delta\lambda/\lambda = 6\%$. Rheo-USANS experiments were performed by positioning an Anton-Paar MCR-301 stress-controlled rheometer equipped with a titanium 30 mm cup and a 29 mm bob between the monochromator and analyzer crystals in the neutron beamline and aligned in the flow-vorticity (1–3) plane. A vertical slit was used to collimate the neutron beam in the USANS, where any evidence of shear-induced anisotropy in the scattering is masked due to slit smearing. De-smearing is not possible for our suspensions with the selected q -range; nevertheless, this does not affect the qualitative analysis presented in this work. Details of the instrument design, setup, and effect of slit smearing can be found elsewhere.³⁹⁻⁴¹ Prior to the neutron scattering measurements, preshear protocols, and steady shear rheology were performed in a similar manner as described in Sec. 2.2, where the shear steady rheology agrees with that from the off-beamline AR-G2 measurement. Neutron scattering from the suspensions at each of the shear stresses measured (1000, 500, 50, 1, 0 Pa for bare silica suspension; 1000, 500, 100, 20, 1, 0 Pa for PEGylated silica suspensions) was collected for 300 min each. Simultaneous rheological measurements were recorded at each stress level during the neutron scattering measurement.

USANS yields a one-dimensional scattering profile with the detector aligned along the flow direction that is a slit-smearred average over an anisotropic scattering pattern in the velocity–vorticity (1–3) plane of flow at different stresses. Data reduction followed the standard procedures using the IGOR Pro reduction macros. The SASVIEW software

package⁴² was used to fit the static USANS data using a hard sphere (HS) model for bare silica and a core-shell hard sphere (CSHS) model for PEGylated silica with consideration of the slit-smearing effect.

2.4 Rheo-VSANS measurements

Very-small angle neutron scattering (VSANS) was performed on the NG3 vSANS diffractometer with q -range from $5 \times 10^{-4} \text{ \AA}^{-1}$ to $1.2 \times 10^{-1} \text{ \AA}^{-1}$, $\lambda = 6.7 \text{ \AA}$, $\Delta\lambda/\lambda = 12\%$, and a 2 mm circular aperture. Rheo-VSANS experiments were performed by an Anton Paar MCR-501 stress-controlled rheometer equipped with a titanium 29 mm cup and a 28 mm bob. The Rheo-VSANS setup was positioned at the center of the Couette geometry in the flow-vorticity (1–3) plane in the beamline. Prior to the neutron scattering measurements, preshear protocols and shear steady rheology were performed in a similar manner as described in Sec. 2.2. Neutron scattering measured from the PEGylated silica suspensions at different stress levels (1000, 900, 800, 700, 600, 500, 200, 100, 50, 10, 1, 0 Pa) was collected for a 60 min interval followed by a 100 s interval of transmission measurements. Shear viscosity measurements with 2D scattering spectra were simultaneously collected. Data reduction followed the standard procedures using the IGOR Pro reduction macros.

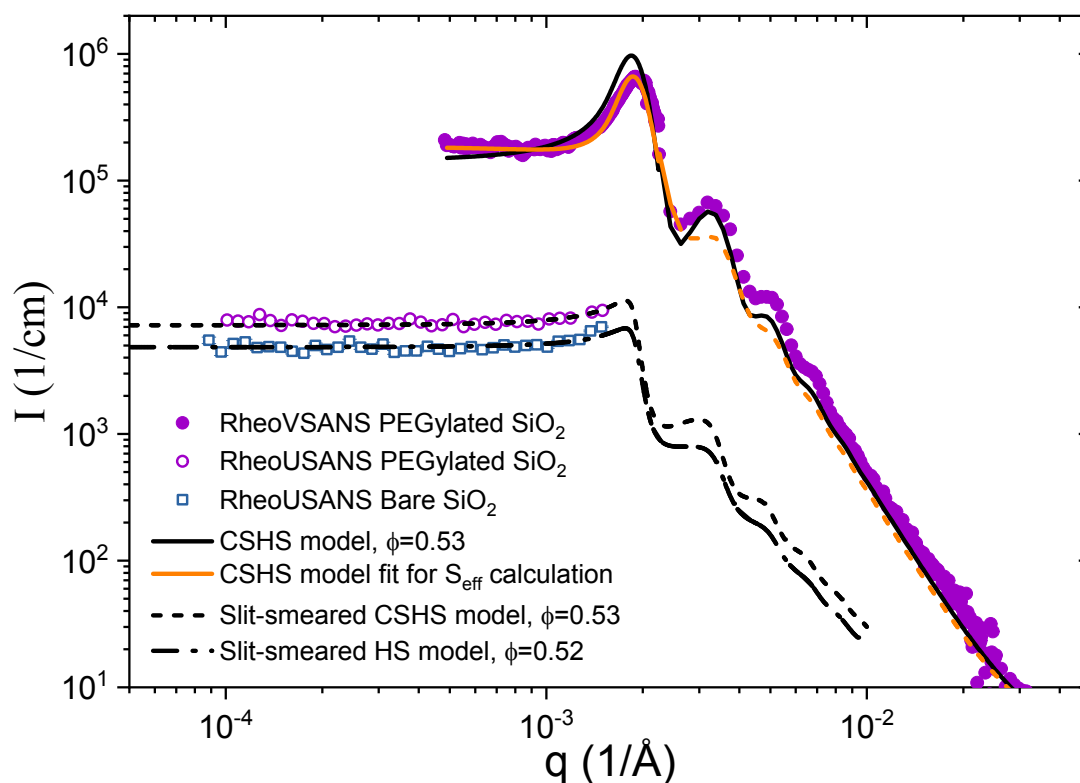


Figure 1 1D VSANS and USANS results as a function of scattering vector q for bare and PEGylated silica suspensions in 1 mm path length Couette shear cell. Dash line: Slit-smearing CSHS model fit for USANS results of PEGylated silica suspension. Dash dot line:

Slit-smearred HS model fit for USANS results of bare silica suspension. Line: CSHS model prediction for VSANS using the same parameters used in USANS. All parameters used are listed in Table I. Orange line: CSHS model fit for calculation of the effective structure factor in the q -range from $4.9 \times 10^{-4} \text{ \AA}^{-1}$ to $2.6 \times 10^{-3} \text{ \AA}^{-1}$ with released constraints of polydispersity and SLD difference, where gray dash line represents the calculated extension values from the fit.

2.5 SANS modeling and analysis

The combination of Rheo-USANS and Rheo-VSANS probes particle properties from length scales spanning nanometers to $\sim 60 \text{ \mu m}$ (dimension of ~ 100 particle diameters), which enables studying particle surface properties and particle spatial arrangements, including hydroclustering under shear. The measured scattering intensity, $I(\mathbf{q})$, follows:

$$I(\mathbf{q}, \sigma) = \phi(\Delta\beta)^2 V_p P(q) S(\mathbf{q}, \sigma, \phi) + I_b. \quad (1)$$

In Eq. (1), ϕ , $\Delta\beta$, V_p , I_b are the volume fraction of the scattering objects (here, silica nanoparticles), the difference of scattering length densities between the particle and the solvent, the volume of the particle, and the incoherent background scattering, respectively. $P(q)$ is the form factor of the scattering particles, reflecting size, shape, and polydispersity of the particles. $S(\mathbf{q}, \sigma, \phi)$ is the structure factor, reflecting the spatial distribution of particles in suspension under shear stress, associated with the Fourier transform of the pair correlation function, $g(\mathbf{r})$. As will be shown, quantitative fitting of the measurements can be achieved with parameters that are determined independently or are highly constrained by physical considerations, lending confidence in the veracity of the results and the parameters extracted from the fitting.

Equilibrium VSANS and USANS measurements for bare and PEGylated silica suspensions are shown in Figure 1. The low intensity plateau in the low- q regime of USANS is indicative of the excluded volume of near-hard sphere dispersions, which further indicates good dispersibility of the two suspensions as any aggregation would lead to an increased intensity. The difference between VSANS and USANS spectral intensities is due to the slit smearing arising from the slit scattering geometry of the USANS instrument.³⁹ The same fit model is shown for both experimental conditions with the requisite slit smearing incorporated for the rheo-USANS measurements, enabling quantitative comparison between experiments in terms of the measured intensities. The effective volume fraction determined from the high shear viscosity plateau and calculated number averaged radius from DLS were used in the model fitting. The thickness of the PEGylation coating was assumed to be equal to the averaged contour lengths of PEG (6-9 units) chains using 0.318 nm for the length of a segment unit of PEG.⁴³ As silica particles contain finite porosity, where solvent penetration

may alter the apparent SLD of particles, the apparent SLD for both particles is determined from the HS or CSHS model fit to the USANS data, yielding $\beta_p=2.80\times 10^{-6} \text{ \AA}^{-2}$ for bare silica and $3.33\times 10^{-6} \text{ \AA}^{-2}$ for PEGylated silica. Comparing this SLD value determined for bare silica to the value of $3.44\times 10^{-6} \text{ \AA}^{-2}$ calculated from the skeletal density indicates 22% of the particle volume can be accessed by the solvent. For PEGylated silica, the apparent SLD is higher because the grafted organic coating blocks some fraction of the internal pores preventing solvent penetration. These observations, along with the calculated porosity, are in line with values from literature.³⁶ Using the SLD from the USANS fit, good agreement between the VSANS data of the PEGylated silica suspension and the CSHS prediction validates the parameters listed in Table I, indicating $\phi_{\text{eff},\infty}$ and the fitted SLD are reasonable.

To investigate the spatial distribution of particles in suspension under flow, an effective nonequilibrium structure factor is calculated using the following equation,

$$S_{\text{eff}}(q, \mathfrak{R}) = \langle S_{\text{eff}}(q, \theta, \mathfrak{R}) \rangle = \frac{\langle I(q, \theta, \mathfrak{R}) \rangle - I_b}{\phi(\Delta\beta)^2 V_p P_{\text{eff}}(q)}. \quad (2)$$

The bracket operator represents the average in the θ -direction (i.e., circular average of the 2D detector), P_{eff} is the effective form factor with consideration of polydispersity. The average transmissions are 0.93 and 0.29 in the Rheo-USANS and Rheo-VSANS measurements, respectively, such that multiple scattering is an issue for the latter.^{21, 25} As multiple scattering unevenly contributes to the intensity throughout the q -range measured, there is no analytical method to correct for the effect. To accurately calculate the effective structure factor, instead of using the form factor using the parameter listed in Table I, we use an empirical model fit (orange line in Figure 1) with released constraints of polydispersity and SLD difference to better capture the measured equilibrium structure in the low q -range of interest for use in obtaining P_{eff} for Eqn. (2), so as not to introduce spurious quantitative errors arising from small discrepancies between the model and data arising from multiple scattering.

3 Results and Discussions

3.1 Steady shear rheology

The steady shear rheology was performed in Rheo-VSANS, Rheo-USANS, and off-beamline measurement with a cone and plate geometry. The corresponding flow curve is described by the relative viscosity, $\eta_r=\eta/\eta_m$, as a function of shear stress, as shown in Figure 2. Both suspensions exhibit the typical shear thinning and thickening response of a dense colloidal suspension, while a significant difference in the extent of shear thickening is observed between bare and PEGylated silica suspensions, indicating the organic coating suppresses hydrodynamic interactions between particles that promote shear thickening.⁴⁴

Shear thinning behavior at the measured lowest shear rate is due to colloidal forces including Brownian motion, but such interactions will not affect our analysis in the shear thickening region. A well-defined high shear viscosity plateau is observed for both suspensions prior to the onset of shear thickening. This high shear plateau viscosity (minimum viscosity) is denoted as $\eta_{r,\infty}$, and this value is used to calculate the effective hard sphere volume fraction $\phi_{\text{eff},\infty}$,³⁸ where $\phi_{\text{eff},\infty}=0.52$ for bare silica and $\phi_{\text{eff},\infty}=0.53$ for PEGylated silica as listed in Table I. Rheological measurements between a cone and plate geometry with ARG2 and a Couette cell with MCR301 agree well with each other for both bare and PEGylated samples. An increasingly negative first normal stress difference, N_1 , accompanies shear thickening. These results are further confirmed with selected 30 min peakhold measurements as shown as points with uncertainties representing the N_1 fluctuations. The time-resolved data for the peakhold measurements are documented in the supplementary materials.

In the following, the rheological measurements for shear stress and normal stress in the continuous shear thickened state are compared against predictions of a friction contact model¹⁴ to estimate the effective contact friction for the two dispersions. Further comparisons are made against enhanced lubrication hydrodynamics simulations^{7, 8} and measurements on similar suspensions from literature.

The semi-empirical friction contact model of Singh et al.¹⁴ is used to estimate the effective interparticle friction coefficient, μ_{fit} , by fitting the model to the flow curve after the onset of shear thickening, yielding $\mu_{\text{fit}} = 0.60$ for the bare silica suspension and $\mu_{\text{fit}} = 0.14$ for the PEGylated silica suspension. Note that there is a difference between the experimentally measured and theoretical onset stresses in definition. The experimental onset stress of shear thickening, σ_{onset} , is typically taken at the stress where minimum of viscosity occurs before shear thickening, while the theoretical onset stress used in the model is the stress where $e^{-1} = 0.37$ of the contacts are frictional. In this work, the theoretical onset stress used in the model is chosen as $8\sigma_{\text{onset}}$, where the empirical factor of 8 agrees with previous observation.^{15, 45} Shear thinning behavior at low shear rates is not captured by the model of Singh et al. because the model does not consider the Brownian or other colloidal interactions, which contribute to the viscosity at low shear rates.¹ It is noteworthy that the flow curve is fitted to the friction contact model to estimate an effective particle-contact friction coefficient, but rigorous validation would also require congruence of the first and second normal stress coefficients.¹⁵ The effective friction coefficient determined by the fit qualitatively agrees with expectations from lateral microscopy force measurements in literature,⁴⁶ showing that a polymer coating can successfully lubricate the particle surface and hence reduce the tangential interactions between particles, which suppresses the shear thickening. The prediction of the model of Singh et al. for N_1 is for the nearest friction coefficients available

in their model, $\mu=1$ and $\mu=0$ for bare and PEGylated silica suspension, respectively. Singh et al.'s model at $\mu=1$ predicts increasing positive N_1 with shear stress for bare silica suspension, whereas at $\mu=0$ the model predicts negative N_1 for the PEGylated silica suspension. To summarize this comparison, we fit Singh et al.'s model to the shear viscosity for both suspensions in the shear thickened regime and obtain physically reasonable values of friction coefficient. However, the model fails to quantitatively describe the first normal stress difference, as has been observed in prior comparisons,¹⁵ and so these values should be taken as qualitative rather than quantitative indications that the bare silica particles exhibit some level of contact friction in the shear thickened state whereas the PEGylated particles do not.

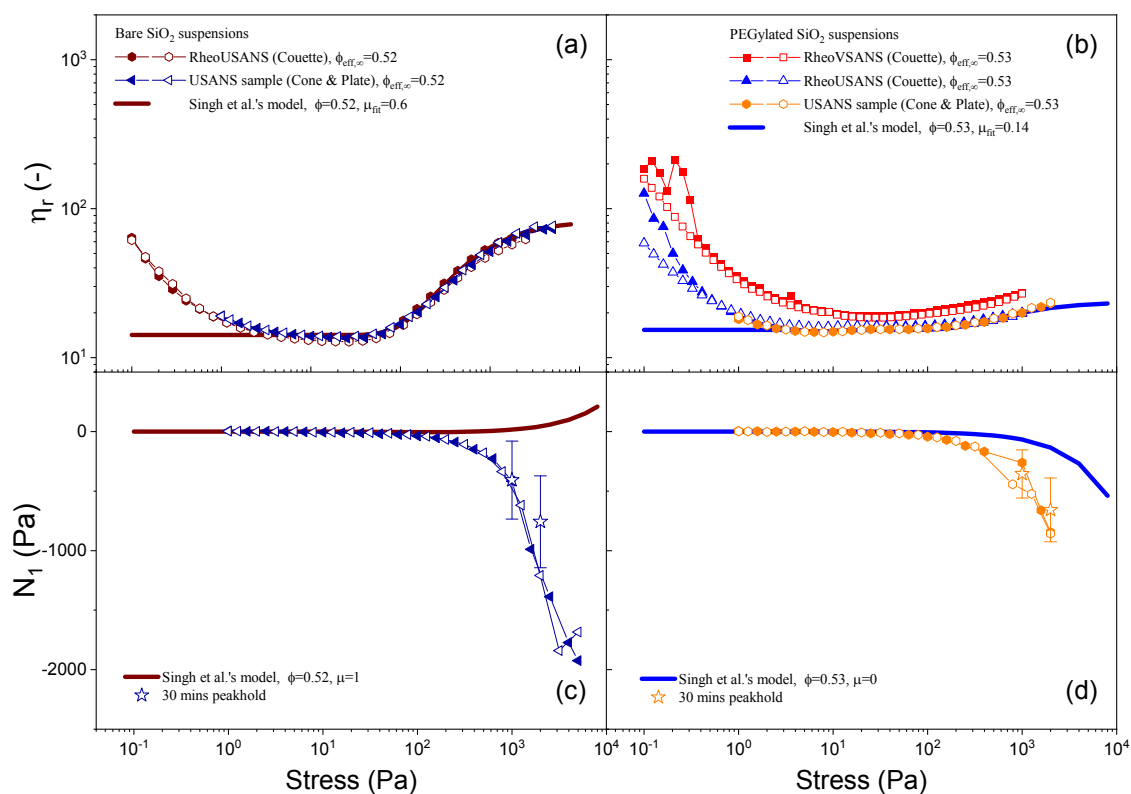


Figure 2. Relative viscosity and first normal stress difference as a function of shear stress for bare (a and c) and PEGylated (b and d) silica suspensions. Filled symbols: forward flow sweeps. Open symbols: backward flow sweeps. Open stars: 30 min peakhold measurement with error bars reflecting the fluctuation of N_1 over time. Effective hard sphere volume fractions are determined using the high shear viscosity of each flow curve. Lines are the prediction of Singh et al.'s constitutive model¹⁴ using the corresponding $\phi_{\text{eff},\infty}$ for each flow curve with varied μ_{fit} . The theoretical onset stress for the model is chosen as $8\sigma_{\text{onset}}$.

Comparisons of the rheological measurements with simulation results of Seto and Guisteri⁴⁷ for suspensions with contact friction and Wang et al.⁷ for enhanced lubrication

hydrodynamics are shown in Figure 3, along with experimental results for near hard sphere dispersions without contact friction⁵ and suspensions of bare particles by Royer et al.⁴⁸ and Cheng et al.²⁶ as appropriate. The material properties in the continuous shear thickened state from all data are listed in Table II. The systems are selected at the nearest comparable volume fractions and grouped according to the nature of the surface (bare or stabilized). Some general results are apparent when the results are compared in dimensionless form as relative viscosity η_r and first normal stress difference coefficient $\Upsilon_1 = -N_1/\eta_m \dot{\gamma}$ for suspensions as a function of the shear stress normalized by the critical stress σ_{onset} at the onset of shear thickening.

The onset stress of shear thickening (the minimum of viscosity) is used to normalize the shear stress and enable comparisons across experimental systems, models, and theory, while the viscosities are plotted as relative viscosities, yielding dimensionless coordinates. The suspension of bare silica particles shows a comparable shear stress, but larger magnitude of negative normal stress, in the shear thickened state as compared to the published results of Royer et al.⁴⁸ for a similar suspension of bare silica particles in a small molecule mixed aqueous/organic solvent. The measured first normal stress coefficients are also greater than predictions by models or either simulation method, as well as the values in the shear thickened state for near hard spheres as determined by Cwalina and Wagner.⁵ The drop in Υ_1 observed at $\sigma/\sigma_{\text{onset}} > 100$ may indicate a transition from hydrodynamic-dominated to frictional-dominated shear thickening, also reported in Royer et al.⁴⁸ Dilation^{49, 50} may play a role here, but confirmation of dilation requires further careful work in monitoring the air-suspension interfaces.⁵¹

For the suspension of PEGylated silica particles, only a very weak shear thickening is observed, as anticipated. Further, the first normal stress difference coefficient shows qualitatively similar behavior to literature results on comparable systems. Models dominated by interparticle friction are unable to represent the measured first normal stress coefficient despite fitting the viscosity, while the enhanced hydrodynamic model qualitatively predicts the negative N_1 in the shear thickened state for both dispersions, but underpredicts the magnitude of the first normal stress difference coefficient for the suspension of bare silica and overpredicts the magnitude for the PEGylated silica suspension. Further inspection of Table II shows the limiting values of Υ_1 in the shear thickened state for the PEGylated silica suspension lies within values typically reported for many systems, whereas the much larger value for the bare silica suspension lies above.

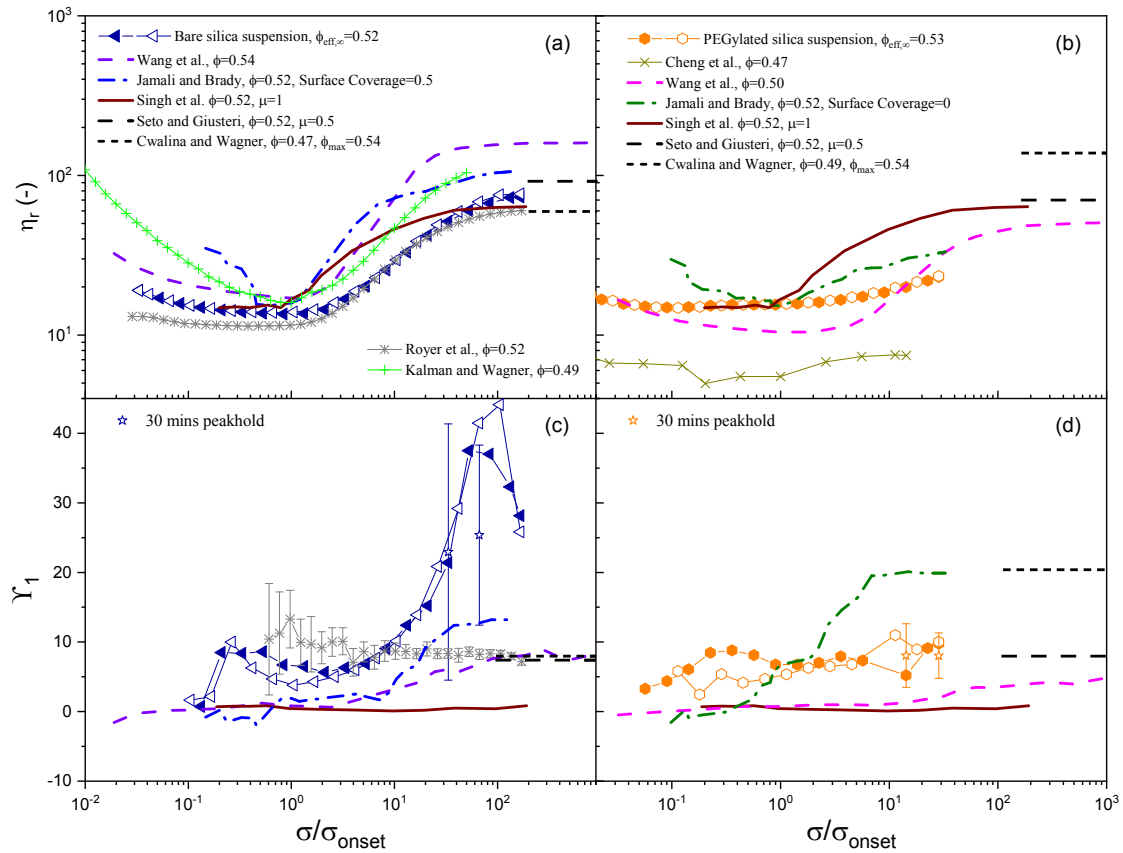


Figure 3. Normalized relative viscosity and first normal stress difference coefficient of bare (a,c) and PEGylated (b,d) silica suspension as a function of normalized shear stress. Both experimental^{5, 26, 35, 48} and computational^{7, 8, 14, 47} work from literature at similar volume fractions are properly compared. The stresses where minima viscosity happen before shear thickening are chosen as the onset stress for each flow curve.

Table II: Comparison of relative viscosity and first normal stress difference coefficient at shear thickened between experimental and computational results.

| | ϕ | $\eta_{r,STS}$ | $\Upsilon_{1,STS}$ or $\frac{-N_1}{\eta_r \dot{\gamma}} (Pe \rightarrow \infty)$ | Methods |
|---|--------|----------------|--|--|
| Bare silica suspension (This work) | 0.52 | 77 | 56 ± 5 | Linear analysis around the shear thickened state |
| PEGylated silica suspension (This work) | 0.53 | 23 | 10.2 ± 3.5 | Linear analysis around the shear thickened state |
| Singh et al. 2018 ¹⁴ | 0.52 | 64 | 0.85 | Friction contact simulation with $\mu = 1$ |
| Seto et al. 2018 ⁴⁷ | 0.52 | 70 | 7.5 ($\mu = 0.5$) | Friction contact simulation |
| | | 136 | 7.2 ($\mu = 1$) | |
| Wang et al. 2020 ⁷ | 0.54 | 160 | 8.1 ($\alpha = 0.04$) | Spectral Ewald Accelerated Stokesian Dynamics |
| | 0.50 | 51 | 4.8 ($\alpha = 0.013$) | |
| Jamali and Brady, 2019 ⁸ | 0.52 | 33 | 12.7 (surface coverage=0) | Dissipative Particle Dynamics simulation with asperity size of $0.05a$ |
| | | 105 | 8.44 (surface coverage=0.5) | |
| Cwalina and Wagner, 2014 ⁵ | 0.470* | 59.5 | 7.98 | Semi-empirical correlation assuming $\phi_{max} = 0.54$ |
| | 0.494* | 138 | 20.4 | |

*Volume fraction computed from skeletal density is reported to stay consistent with the definition of volume fraction from Cwalina and Wagner.

3.2 Investigating microstructure of PEGylated suspensions using Rheo-VSANS and Rheo-USANS

Rheo-VSANS and Rheo-USANS microstructure measurements taken during steady shear for the PEGylated silica suspension are reported in Figure 4(a). Static measurements at 0 Pa and the CSHS model fit from Figure 1 are also shown, serving as the baseline for comparison between measurements under shear. The predominant features evident in the measured Rheo-VSANS spectra are the increased intensities with stress in the medium q-range (from 0.0005 to 0.0015 \AA^{-1} , grey shaded area), while no effect is observed at higher-q. This former observation in the medium q-range covers microstructure spanning from 0.42 to 12 μm or 1.1 to 32 particle diameters, indicating particle clustering under shear flow. Such features are associated with the change in the structure factor. The latter observation demonstrates that particle integrity is maintained throughout the experiment.

Particle clustering under shear^{4, 17, 24} and the resulting increased scattering intensity under shear in the medium q-range has been reported in previous SANS experiments.^{24, 25, 35, 52} This increased intensity can also be observed in Rheo-USANS measurements in the same q-range. In a lower q-range (from 0.0001 to 0.0005 \AA^{-1} , green shaded area), the intensity profiles tend to converge to a common plateau value independent of shear rate, suggesting an upper bound to the size of the hydrocluster formation. A calculation of the average intensity under shear normalized by the average of the intensity at rest for the q-range is shown in panel (d), which also supports these observations.

The increasing intensity with stress agrees with confocal microscopy observations under shear flow by Cheng et al.²⁶, where visual information on particle positions is transformed to cluster probability distributions. The cluster probability distribution itself depends upon the contact criterion selected. Here, the assumption is made that the choice of the contact criterion should not affect the qualitative trend of the increased cluster probability distribution with increased shear stress. Rigorous examinations of the effect of choice of contact criteria can be found from Pradeep and Hsiao.⁵³ The cluster probability distribution can then be converted to estimates of scattering intensity, as documented in the supplementary material. This calculated scattering intensity derived from the confocal microscopy shows a similar trend of increasing intensity with stress, in qualitative agreement with our SANS results.

Further analysis for elucidating this shear-induced structure formation is also shown in Figure 4(b) and (c), representing the subtraction of the intensity under shear from that at rest for VSANS and USANS measurements, respectively. As can be observed in Figure 4(b), the increasing shear flow results in the development of a broad correlation peak at $q_{\text{max}} \sim 0.0016 \text{\AA}^{-1}$ (corresponding to a scale of 1.1 particle diameter in real space). The growth of the

intensity becomes more distinct at the onset stress of shear thickening (50 Pa), and it tends to saturate at higher shear stress. Similar results are observed for USANS in Figure 4(c), where the correlation peak is located at $q_{\max} \sim 0.0013 \text{ \AA}^{-1}$ (scale of 1.3 particle diameter in real space). In general, from our scattering results, the cluster structure is found to be highly localized and consisting of only a few highly-correlated particles. This observation agrees with Cheng et al., where 85% of hydrocluster structure contain three or fewer particles when suspensions shear thicken. Figure 4(d) compares the general trend of increasing scattering intensity from experiment with an estimate of the scattering intensity expected from the cluster distributions reported by Cheng et al., calculated using an assumed fractal dimension of 2.5.

To further investigate the microstructure features responsible for the source of the increased intensity, the effective structure factors under flow, calculated via Eq. (2), are shown in Figure 5(a). The structure factor predicted for the HS potential shows good agreement with the calculated effective structure factor at equilibrium. The effective structure factor under flow evolves systematically with shear stress in the medium q -range (grey area), where similar behavior is also observed in the USANS measurements of Kalman and Wagner³⁵ for a coated silica suspensions exhibiting stronger shear thickening (shown in Figure 3(a)) at a comparable volume fraction. A $\sim 60\%$ increase of scattering intensity around $qa \sim 1$ can be observed for effective structure factor measured at 1000 Pa compared to the equilibrium effective structure factor.

Simulation results for the structure factor from the friction contact model¹² and enhanced lubrication hydrodynamics model,⁷ however, both show a significant, qualitative difference in microstructure as compared with experiments as evident in Figure 5(b). Both models overpredict the structure build-up at lower q with a peak value around $qa \sim 0.6$ (corresponding to 5.2 particle diameters), suggesting the existence of a longer-range correlation independent of the micromechanical mechanism driving the increase in shear viscosity. Note that the structure build-up at lower q is independent of the projection of the shear plane for structure factors available from both models, so only one-dimensional data extracted from the 2D structure factors in the 1-3 shear plane are presented for comparison. For the friction contact simulation, this long-range structure correlation also exists before the onset of shear thickening, which makes structure factors between low and high shear states indistinguishable. However, the enhanced lubrication hydrodynamics model shows an increase in structure formation at low- q with the onset and growth of shear thickening in qualitative agreement with the experimental results.

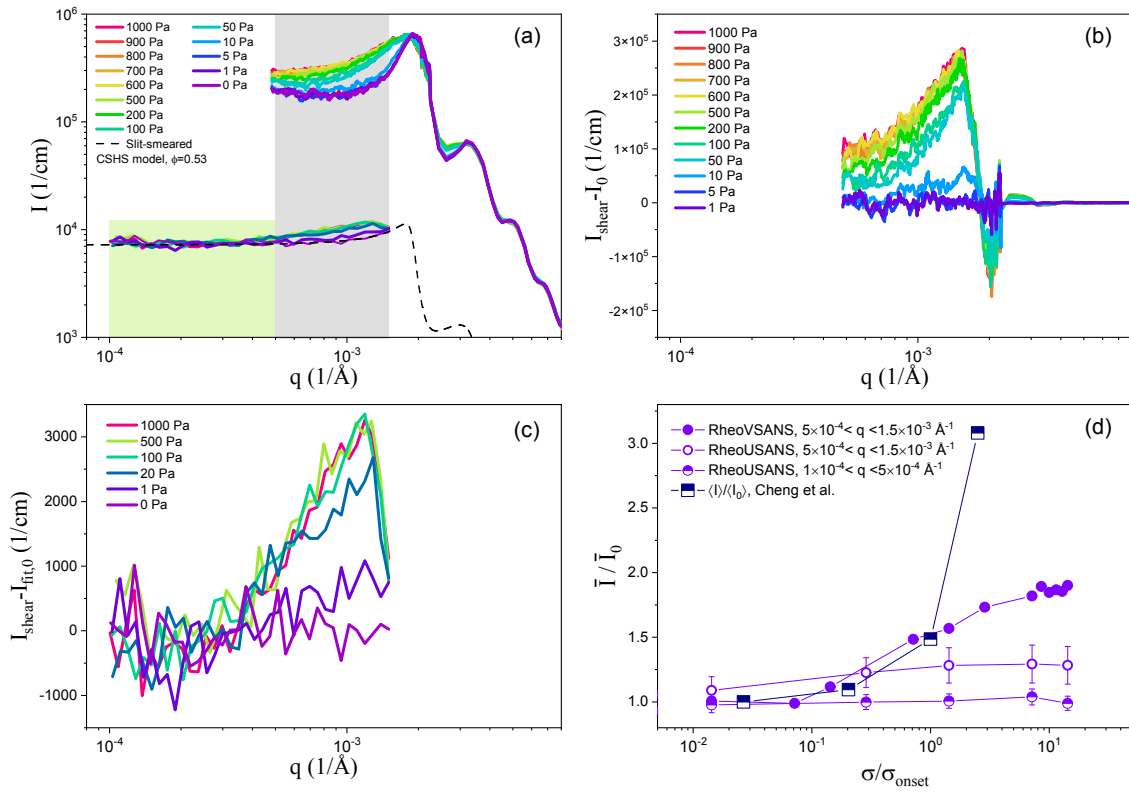


Figure 4. (a) 1D scattering measurements of Rheo-VSANS and USANS at varied shear stress for PEGylated silica suspension. Dash line: slit-smeared CSHS model fit for USANS results of PEGylated silica suspension. (b) $I(q)$ data of Rheo-VSANS under shear subtracting the static measurement $I_0(q)$ at 0 Pa. (c) $I(q)$ data of Rheo-USANS under shear subtracting the polynomial fit $I_{\text{fit},0}(q)$ of the static measurement. (d) Averaged values of intensity over the grey and green shaded area in (a) as a function of shear stress, where the values were normalized by the averaged value at 0 Pa. Error bars reflect the standard deviation over the specified q -range. Estimated scattering intensity from confocal measurements in Cheng et al.²⁶ is also reported, assuming a fractal dimension of 2.5 for the internal structure of hydroclusters.

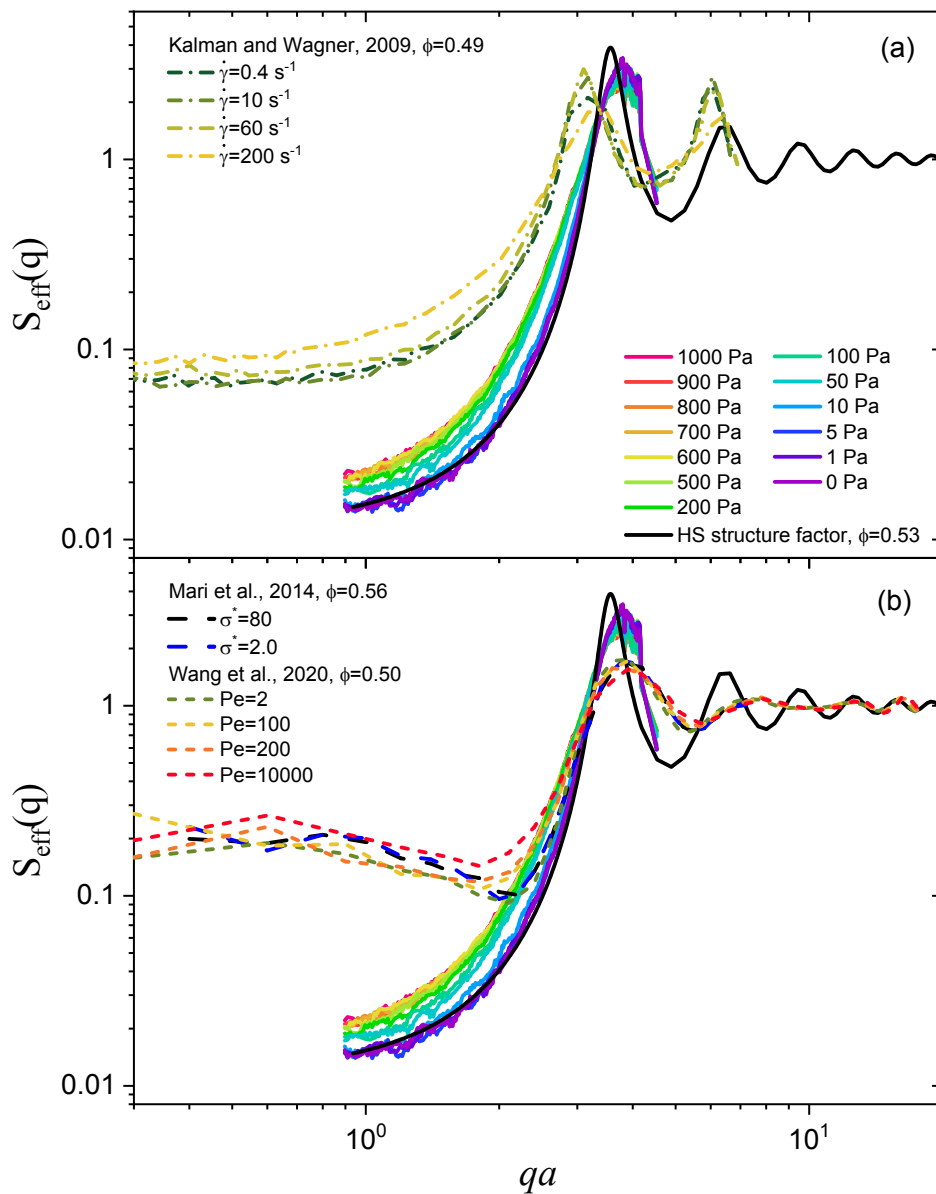


Figure 5. Effective steady shear structure factors measured by Rheo-VSANS for PEGylated silica suspension in comparison with (a) experimental data from Kalman and Wagner³⁵ and (b) simulation results from Mari et al.¹² and Wang et al.⁷ Black solid line: the hard sphere structure factor theoretical prediction using parameters listed in Table I. Dash dot lines: Rheo-USANS results from Kalman and Wagner.³⁵ Dash lines: simulated structure factors from Mari et al.¹² before (blue) and after (black) the onset of shear thickening. Short dash lines: simulated structure factors from Wang et al.⁷ with various Peclet numbers, where the onset of shear thickening occurs at $Pe=200$. Note that, for both simulation results, data are extracted from structure factors in the 1-3 shear plane, and that q is normalized by the volume average radius of the bidisperse system. The grey area represents the same medium q -range defined in Figure 4(a).

To quantify the shear-induced microstructural changes evident in Figure 5, the structure factor at rest S_{eq} is subtracted from S_{eff} under shear. The resultant peak is analyzed using a broad peak model, as illustrated in Figure 6(a) using the following equation,

$$\langle S_{eff}(q, \theta, \xi) \rangle - S_{eq}(q) = \langle S_{noneq}(q, \theta, \xi) \rangle = \frac{S_{peak}}{1 + (q - q_{peak})^2 \xi^2}. \quad (3)$$

The value of subtraction can be treated as the nonequilibrium structure factor, S_{noneq} , resulting from the shear-induced hydrocluster structure. Such nonequilibrium structure is described by the broad peak model with three parameters: the scale of the structural peak S_{peak} , the peak position q_{peak} , and the correlation length ξ . The peak position is chosen at $q_{peak} = 0.0016 \text{ \AA}^{-1}$ and the value of correlation length can be calculated from the model fit as shown in Figure 6(b). We note that the experimental evidence for hydrocluster formation for stresses below 50 Pa is not of sufficient resolution to generate statistically meaningful fits. Therefore, just for comparison we show a fit using the measurable value $\xi = 540 \text{ nm}$ from the first statistically meaningful fit to show that this size scale can represent the effective structure factor at 10 Pa. Note that only half of the structural peak is fitted to the broad peak model due to the interference from the structure factor peak at the higher q -values, which is the primary interparticle correlation peak. The value of S_{peak} , which is related to the extent of hydrocluster formation, increases with shear stress, in qualitative agreement with expectation. Meanwhile, the fitted correlation length decreases with shear stress and saturates at 450 nm (~ 1.2 particle diameter), indicating the finite size of hydrocluster formation with developing shear stress.

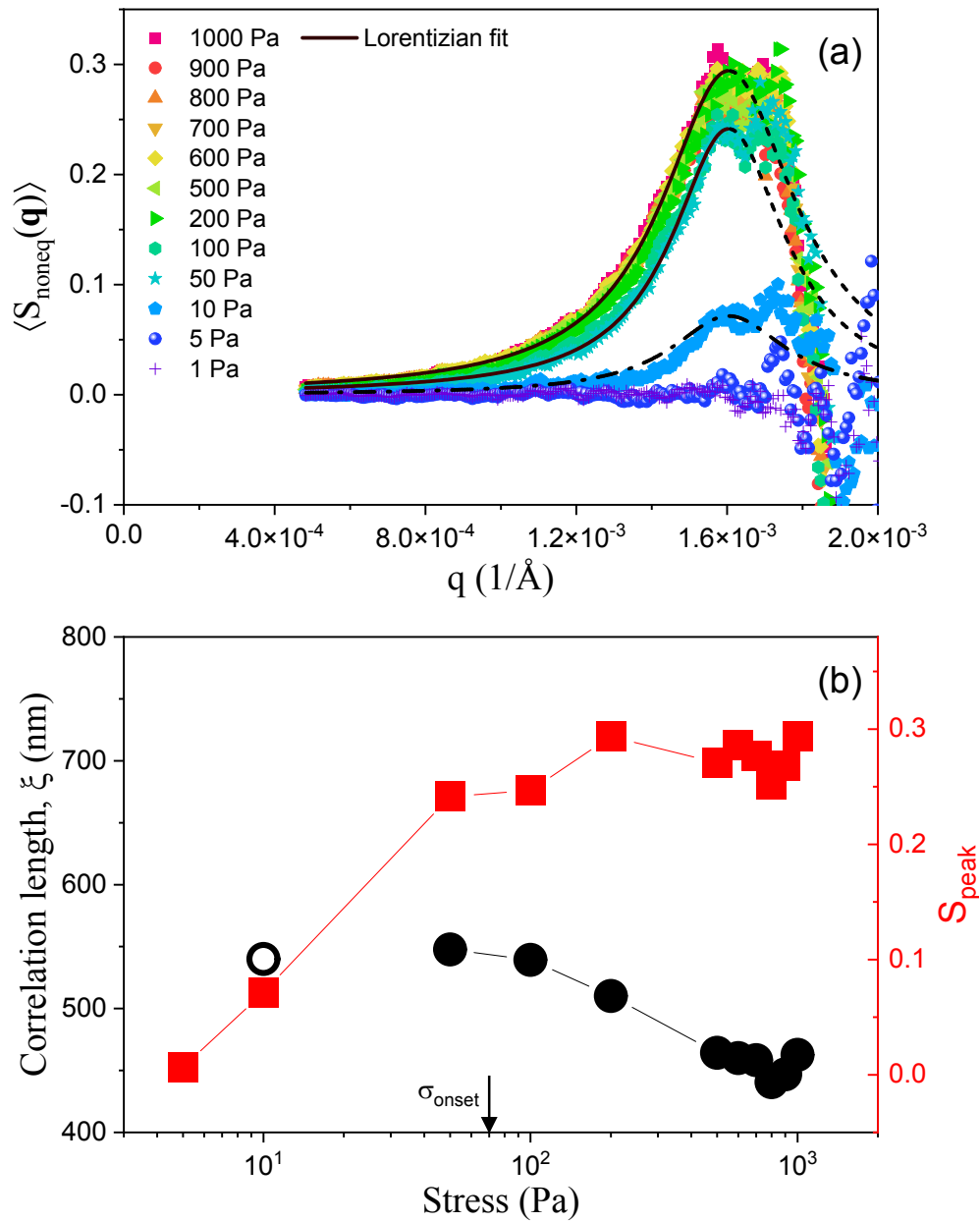


Figure 6. (a) Nonequilibrium structural factor as a function of scattering vector with varied shear stress. Only half of the structural peak ($q_{\text{peak}}=0.0016 \text{ \AA}^{-1}$) is fitted to the broad peak model, where lines represent the model fit and dash lines represent the extension of the model fit. Only two model fits for the stresses of 1000 and 50 Pa are shown here for clarity. Dash dot line is the model prediction assuming $\xi=540$ nm. (b) The scale of the structural peak and fitted value of correlation length as a function of shear stress. Error bars are smaller than the black symbols presented. Open black symbol shows the fixed value of the size used to extract the peak height for the lowest stresses (see text).

3.3 Anisotropic microstructure and stress-SANS analysis

Anisotropic microstructures are frequently observed in shear thickening colloidal suspensions, where the nature of anisotropy contributes to the highly non-Newtonian behavior of suspension rheology.^{21, 54} To investigate the microstructure-stress relationship, the stress-SANS rule has been established to quantitatively connect the microstructure measured by SANS and the rheological stress response of dispersions under flow. The 3D microstructure of suspension under flow can be described using a spherical harmonic expansion. On the projected plane of interest (velocity-vorticity plane in this work), the 3D harmonic expansion of the structure factor is reduced to a Fourier expansion after projection to a 2D plane. The dimensionless structure factor hence can be written as,

$$S_{q-avg}^{gradient*}(\theta, \mathbf{\hat{q}}) = \frac{S_{q-avg}^{gradient}(\theta, \mathbf{\hat{q}})}{S_{q-avg}^{gradient}(\theta, \mathbf{\hat{q}}=0)} = c_0^* + c_2^* \cos 2\theta + c_4^* \cos 4\theta. \quad (4)$$

Coefficients of the Fourier base weighting functions represent the degree of rotational symmetry of the anisotropic microstructure. As the measured scattering plane for the 1-3 configuration in the Couette geometry necessarily exhibits twofold symmetry, there is no contribution of symmetries of $\sin(n\theta)$ for $n=2, 4, \dots$. Details of the derivation can be found in the supplemental materials. Analysis shows that terms up to 4th order symmetry are sufficient to capture the anisotropy in the 1-3 plane probed here, in agreement with prior studies.²¹

Quantitative characterization of the anisotropic microstructure under shear for the PEGylated suspension is provided as the annular average of Rheo-VSANS intensity spectra for the velocity-vorticity plane over the medium q -range as indicated in Figure 7. Highly anisotropic microstructures for shear thickening suspensions have been reported in the literature, where most of the anisotropic features were measured on the velocity-velocity gradient plane. Here, it is found that anisotropy also exists on the velocity-vorticity plane, confirming prior measurements on related systems by Gurnon and Wagner.²¹ With increasing shear stress, the intensity increases along the velocity axis at 0° and 180° (shear direction) and decreases in intensity along the vorticity axis. Such scattering features identify microstructural alignment along the vorticity axis in real space on length scales associated with nearest neighbor particles, in agreement with previous confocal microscopy²⁶ and Flow-SANS^{21, 22} experiments. Microstructural bands aligned along the vorticity axis have also been reported using ultrasound imaging for discontinuous shear thickening cornstarch suspensions.⁵⁵ The degree of anisotropy can be determined by fitting the normalized annular average, $I(q, \theta)/\bar{I}_0$, to Eq. (4) as shown in Figure 8(a) and (b). The first term of Fourier coefficient, c_0^* , is equivalent to \bar{I}/\bar{I}_0 shown in Figure 4(d), representing the extent of the hydrocluster formation. The second term, c_2^* , represents the degree of $\cos(2\theta)$ symmetry, while the aspect ratios, defined by the ratio of the intensity at $0^\circ/180^\circ$ to the intensity at

$90^\circ/270^\circ$, represents the anisotropy of the hydroclusters. Finally, fitting of the Fourier functions shows the contribution of $\cos(4\theta)$ is negligible, that is $c_4^* \sim 0$, regardless of the shear rate. It is observed that c_0^* , c_2^* , and the aspect ratio follows the same trend of monotonic increase with shear stress. Such monotonic increase starts around the onset of shear thickening (70 Pa) and saturates at the highest shear stress measured. These two coefficients quantify the extent of hydrocluster formation and microstructural alignment along vorticity direction in real space, respectively.

To quantitatively connect the microstructure measured by rheo-SANS and the rheological stress response, the stress-SANS rule^{21, 54} can be applied to distinguish stress contributions from thermodynamic stress σ^T , stress from limiting zero shear viscosity, first-order hydrodynamic stress σ_0^H , and higher order hydrodynamic stress σ_4^H . The total stress then can be written as,

$$\sigma^{total}(\dot{\gamma}) = \sigma^T(\dot{\gamma}) + 2\eta_f \dot{\gamma} [1 + 2.5\phi(1 + \phi) + 2.7\phi^2] + \sigma_0^H(\dot{\gamma}) + \sigma_4^H(\dot{\gamma}). \quad (5)$$

To evaluate the thermodynamic stress and higher order hydrodynamic stress, scattering measurements on the velocity-velocity gradient plane are required, which are not accessible given the sample environment used in this work. However, for analyzing the stress contribution around shear thickened state, the thermodynamic stress contribution is negligible as $Pe \sim 120$ at the onset of shear thickening. Thus, the first-order hydrodynamic stress-SANS coefficient for the hydrodynamic stress contribution can be calculated by

$$C_0^{\sigma,H} \sim \frac{\sigma / (2\eta_f \dot{\gamma}) - [1 + 2.5\phi(1 + \phi) + 2.7\phi^2]}{c_0^*(\dot{\gamma})}, \quad (6)$$

where the shear stress and shear rate were determined from rheometry measurements.²¹ Note that the hydrodynamic stress contribution is defined for the SANS condition measured at the largest shear stress in the shear thinning regime (close to the onset stress of shear thickening), so shear condition of 50 Pa gives a constant coefficient $C_0^{\sigma,H} = 4.54$ for the hydrodynamic stress contribution. Once $C_0^{\sigma,H}$ is evaluated, the hydrodynamic stress contribution arising from the microstructure to the suspension viscosity η_0^H is:

$$\eta_0^H = \frac{\sigma_0^H(\dot{\gamma})}{\eta_f \dot{\gamma}} = 2C_0^{\sigma,H} \times c_0^*(\dot{\gamma}). \quad (7)$$

Figure 8(c) compares the stress-SANS results with the rheological measurements from the MCR-501 rheometer. The total stress contribution to the relative viscosity was calculated by adding the limiting zero shear viscosity to η_0^H . The difference between the measurement and the total hydrodynamic contribution is expected to be due to thermodynamic contributions, such as Brownian motion, which dominate at low Pe . After the onset of shear thickening, the stress-SANS rule successfully captures shear thickening in the PEGylated silica suspension, where it is evident that the hydrodynamic stress component contributes to the increased

viscosity. These results indicate that hydrocluster formation and the resulting increase in short-range lubrication hydrodynamic interactions are responsible for continuous shear thickening in the PEGylated silica suspension, further confirming the unimportance of contact friction for this coated suspension under these conditions.

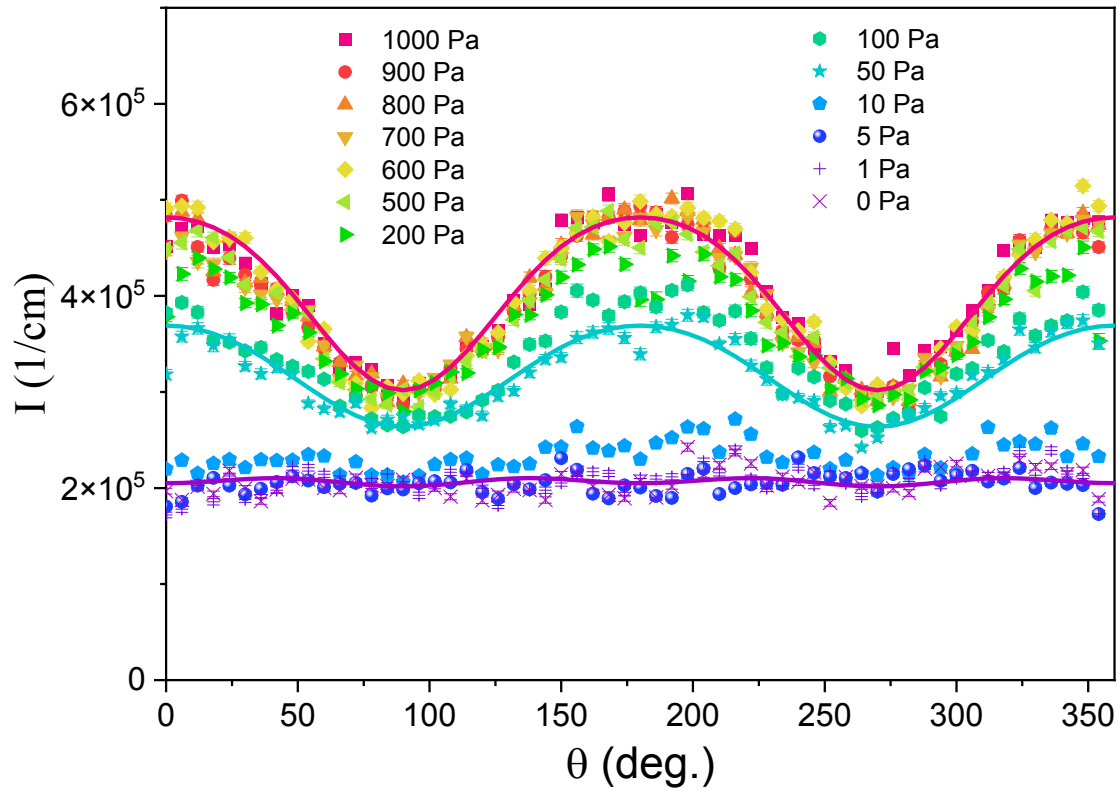


Figure 7. $I(q,\theta)$ averaged over the medium q -range, from 0.0005 to 0.0015 \AA^{-1} , corresponding to the shaded grey area shown in Figure 4(a) for the PEGylated silica suspension. The radial vector aligning with 0° is velocity direction, while the vector aligning with 90° is vorticity direction. Solid lines: the fit to a four-order Fourier expansion at selected shear stresses of 0, 50, and 1000 Pa.

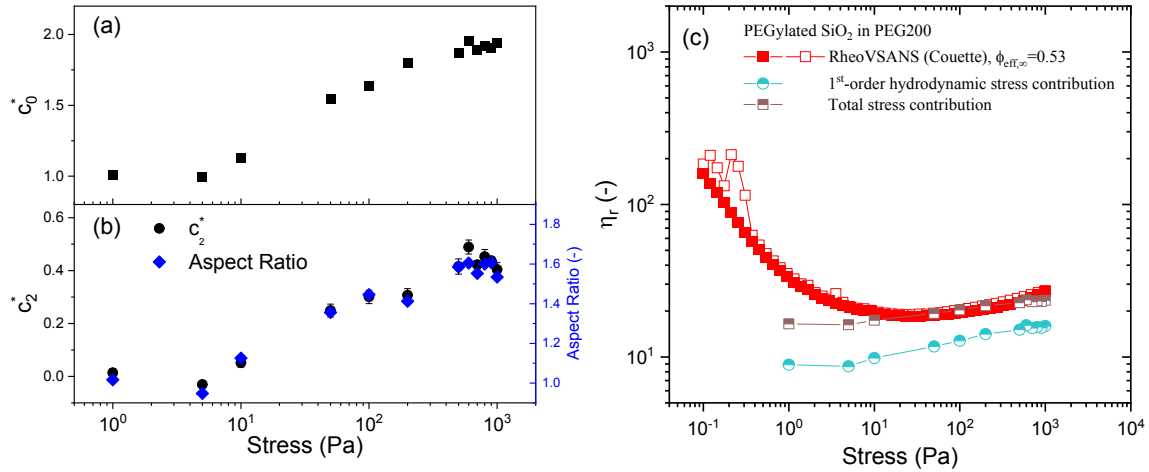


Figure 8. Analysis of the microstructural anisotropy of the PEGylated silica suspension. (a) Fits of Fourier coefficients and (b) calculated aspect ratio as a function of shear stress. Error bars are one standard deviation of the fit error. The aspect ratio was calculated by the ratio of the intensity at $0^\circ/180^\circ$ to the intensity at $90^\circ/270^\circ$. (b) Relative viscosity as a function of shear stress. Red solid and open squares: the rheometry result from RheoVSANS steady shear measurements. Solid symbols represent the forward sweep, while open symbols represent the backward sweep. Half-filled circles: first-order hydrodynamic stress contribution to the relative viscosity calculated using stress-SANS rule. Half-filled squares: total stress contribution to the relative viscosity.

3.4 Rheo-USANS measurements for bare silica suspensions

In contrast to the rheology of the PEGylated silica suspension, a bare silica suspension formulated at a similar weight fraction shows much stronger, but still continuous shear thickening as discussed in Section 3.1. Despite this significant increase in the magnitude of the shear thickened viscosity, qualitatively similar scattering patterns are obtained as for the PEGylated silica suspension as illustrated in panels (a) and (b) of Figure 9. The increased intensity with applied stress in the medium q -range (from 0.0005 to 0.0015 \AA^{-1}) is evident, whereas the intensity tends to converge to a constant in the low q -range (from 0.0001 to 0.0005 \AA^{-1}), again indicating the finite size of the hydroclusters. Subtraction of the intensity under shear from that at rest, shown in panel (b), better illustrates such features, as the increasing shear flow results in the development of a broad correlation peak at $q_{max} \sim 0.0013 \text{ \AA}^{-1}$. Quantitative comparison of the averaged intensities between bare and PEGylated silica suspensions over the low and medium q -range are shown in Figure 9(c). After proper normalization of the shear stress by the onset value of shear thickening, the intensity increase

for the two suspensions is coincidental within reasonable errors regardless of the selected q-range.

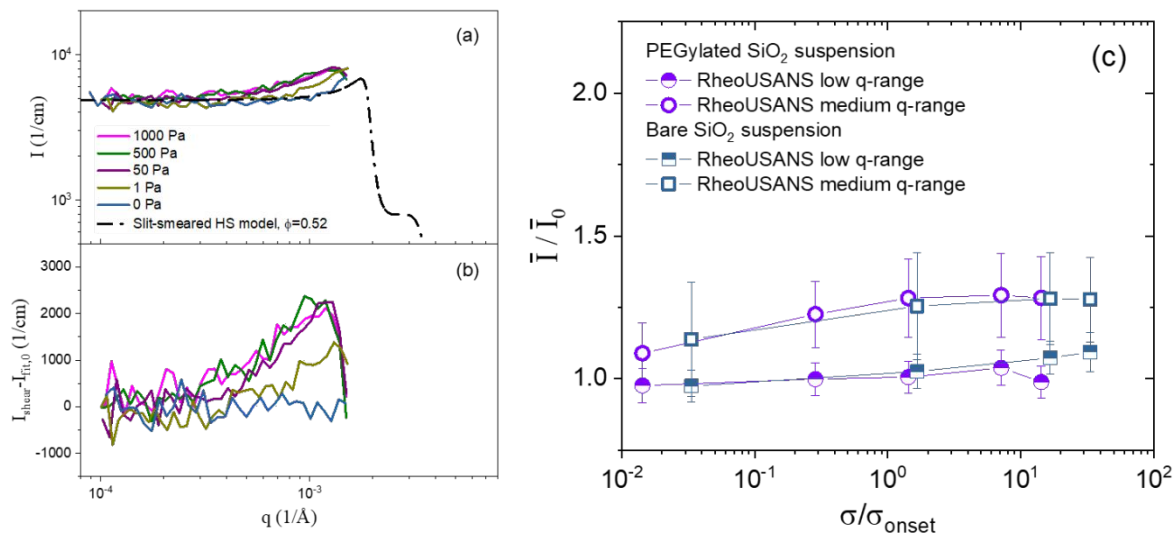


Figure 9. (a) 1D scattering measurements of Rheo-USANS at varied shear stress for bare silica suspension. Dash line: slit-smeared HS model fit with parameters from Table I. (b) $I(q)$ data of Rheo-USANS under shear subtracted from the polynomial fit $I_{\text{fit},0}(q)$ to the static measurement at 0 Pa. (c) Comparison of averaged values of intensity between bare and PEGylated silica suspension over the low (half-filled symbols) and medium (open symbols) q-range as defined in Figure 4. The averaged intensity was normalized by the averaged value at 0 Pa. Error bars reflect the standard deviation over the specified q-range.

While one might be tempted to interpret these observations to indicate that such microstructural measurements cannot distinguish between these very different particle suspensions, it is critically important to recognize that there are very significant differences in the anisotropic microstructure in the 1-2 (velocity-velocity gradient) scattering plane, and that differences in this scattering plane can distinguish between systems with and without contact friction.²⁵ What is shown here are 1-D scattering patterns obtained along the flow direction in the 1-3 plane of flow, and as such, are not able to elucidate any microstructural anisotropy. The experiments designed here complement prior work that developed a quantitative understanding of the detailed internal structure of hydrocluster formation by answering the question as to the *extent* of hydrocluster formation. What is evident for both suspensions is that hydroclusters are very limited in extent in continuous shear thickening suspensions and that simulations show a more distinct and larger hydrocluster formation than observed in experiments, both those reported here and by other methods. Important questions remain, however, about the behavior for more extreme shear thickening suspensions, especially those

that exhibit dilational, discontinuous shear thickening where the force chains become sample spanning,³ which should show up as a longer-range organization of hydroclusters.

4 Conclusion

A study of the size of hydroclusters for two continuous shear thickening suspensions of particles with very different nanoscale interactions is performed by Rheo-USANS and Rheo-VSANS in the 1-3 shear plane. Suspensions at equal weight fractions in the same suspending medium, one of bare Stöber silica particles and one with the same particles but surface PEGylated, show very distinct rheological differences in the shear thickened state. The suspension of bare silica particles shows evidence of possible contact friction, and a value of the friction coefficient is extracted from the model of Singh et al. Meanwhile, PEGylation of these particles is shown to successfully eliminate contact friction. This is also evident from the first normal stress differences for each suspension, which cannot be described by the contact-friction model but are better represented by the enhanced lubrication hydrodynamics model.

For the PEGylated silica suspension, an increase in scattering intensity is observed in the medium q -range (q -values smaller than the primary peak position) as a result of particle clustering on the scale of the particle diameter with increasing stress, commensurate with the increase in shear viscosity. However, the range of hydrocluster formation is very restricted, with estimates of the average cluster size, extracted from the scattering data by multiple methods, being on the order of the particle diameter. These results are observed for both VSANS and USANS experiments, and semi-quantitative agreement is observed with literature reports using SANS³⁵ and direct confocal microscopy measurements under shear on comparable suspensions.²⁶ Rheo-VSANS measurements show a distinct anisotropy development in the 1-3 plane of shear, consistent with vorticity alignment, and in agreement with prior measurements on shear thickening, near-hard sphere colloidal suspensions of coated particles without contact friction,²¹ which complement recent, detailed studies of the anisotropy in the 1-2 plane.²⁵ Importantly, these results combined with the stress-SANS rule²¹ show how this level of hydrocluster formation couples with lubrication hydrodynamics to generate the observed shear thickening viscosity, further confirming the unimportance of contact-friction in this continuous shear thickening suspension of PEGylated silica colloidal particles.

Rheo-USANS experiments comparing the extent of hydrocluster formation for the two colloidal suspensions show no significant difference, showing that the extent and size of hydrocluster formation are similar when the applied stress is normalized by the stress at the onset of shear thickening, despite the large quantitative increase in shear thickening

viscosities of the bare silica suspension relative to the PEGylated silica suspension. It is important to recognize that the 1-D nature of the USANS experiment does not reveal the important differences in the angular distribution of nearest neighbor particles in the hydroclusters, which has been shown to be very sensitive to the nature of the nanoscale forces acting between the particles in the shear thickened state.²⁵ Nonetheless, the measurements shown here support earlier observations in literature that show the size of hydroclusters to be very localized for continuous shear thickening suspensions, and that the size is relatively independent of the nature of the nanoscale forces acting between particles when viewed at comparable dimensionless applied stress in the shear thickened state. Importantly, simulations using contact friction¹² show a distinct cluster formation at a much larger size scale than observed here and the extent of hydrocluster formation is independent of shear stress, which is not in agreement with the experimental measurements shown here. Simulations using the enhanced lubrication hydrodynamic model⁷ also predict a larger size for hydrocluster formation that is comparable to the predictions of contact friction simulations, but the extent of hydrocluster formation grows with stress in qualitative agreement with our observations. While at present it is unknown why both simulation methods, which can semi-quantitatively reproduce the observed shear viscosity, show such distinct formation of hydroclusters of greater size in the shear thickened state relative to a body of experimental observations, we note that other approaches, such as cluster analysis in force space^{56, 57} may better help distinguish the role of hydrocluster formation in the simulations. The results presented here, placed within the context of a growing body of experimental results for the microstructure of continuous shear thickening suspensions, provide experimental evidence that can be useful for the development of better simulation and theory approaches to connecting nanoscale forces to the shear thickened suspension rheology. Further experiments probing the hydrocluster development in discontinuous shear thickening colloidal suspensions and the connection to nanotribology are warranted as percolation of the hydrocluster microstructure is anticipated.

Acknowledgments

The authors would like to thank Paul Butler, Steve Kline, Yun Liu, Jeffrey Richards, and Michael Zhang for valuable discussions for Rheo-SANS data reduction. Mu Wang and Romain Mari are acknowledged for providing simulation results for comparison. The authors acknowledge financial support from The Chemours Company FC, LLC, and the National Institute of Standards and Technology, U.S. Department of Commerce. This manuscript was prepared under Cooperative Agreement No. 370NANB17H302 from the National Institute of Standards and Technology (NIST), U.S. Department of Commerce. Access to the NG3 VSANS instrument and BT5 USANS instrument was provided by the Center for High Resolution Neutron Scattering (CHRNS), a partnership between the National Institute of

Standards and Technology and the National Science Foundation under Agreement No. DMR-1508249. The statements, findings, conclusions, and recommendations are those of the authors and do not necessarily reflect the view of NIST or the U.S. Department of Commerce.

References

1. J. Mewis and N. J. Wagner, *Colloidal Suspension Rheology*, Cambridge University Press, Cambridge ; New York, 2012.
2. N. J. Wagner and J. Mewis, *Theory and Applications of Colloidal Suspension Rheology*, Cambridge University Press, 2021.
3. J. F. Morris, *Annual Review of Fluid Mechanics*, 2020, **52**, 121-144.
4. N. J. Wagner and J. F. Brady, *Physics Today*, 2009, **62**, 27-32.
5. C. D. Cwalina and N. J. Wagner, *Journal of Rheology*, 2014, **58**, 949-967.
6. D. R. Foss and J. F. Brady, *Journal of Fluid Mechanics*, 2000, **407**, 167-200.
7. M. Wang, S. Jamali and J. F. Brady, *Journal of Rheology*, 2020, **64**, 379-394.
8. S. Jamali and J. F. Brady, *Phys. Rev. Lett.*, 2019, **123**, 138002.
9. S. Jamali, A. Boromand, N. Wagner and J. Maia, *Journal of Rheology*, 2015, **59**, 1377-1395.
10. A. Boromand, S. Jamali, B. Grove and J. M. Maia, *Journal of Rheology*, 2018, **62**, 905-918.
11. R. Seto, R. Mari, J. F. Morris and M. M. Denn, *Phys Rev Lett*, 2013, **111**, 218301.
12. R. Mari, R. Seto, J. F. Morris and M. M. Denn, *Journal of Rheology*, 2014, **58**, 1693-1724.
13. M. Wyart and M. E. Cates, *Phys. Rev. Lett.*, 2014, **112**, 098302.
14. A. Singh, R. Mari, M. M. Denn and J. F. Morris, *Journal of Rheology*, 2018, **62**, 457-468.
15. Y.-F. Lee, Y. Luo, S. C. Brown and N. J. Wagner, *Journal of Rheology*, 2020, **64**, 267-282.
16. J. F. Brady and G. Bossis, *Ann. Review Fluid Mech.*, 1988, **20**, 111-157.
17. G. Bossis and J. Brady, *The Journal of chemical physics*, 1989, **91**, 1866-1874.
18. B. J. Maranzano and N. J. Wagner, *The Journal of Chemical Physics*, 2002, **117**, 10291-10302.
19. P. Dhaene, J. Mewis and G. G. Fuller, *Journal of Colloid and Interface Science*, 1993, **156**, 350-358.
20. J. W. Bender and N. J. Wagner, *Journal of Colloid and Interface Science*, 1995, **172**, 171-184.

21. A. K. Gurnon and N. J. Wagner, *Journal of Fluid Mechanics*, 2015, **769**, 242-276.
22. D. P. Kalman, Microstructure and rheology of concentrated suspensions of near hard-sphere colloids, 2010.
23. J. Bender and N. J. Wagner, *Journal of Rheology*, 1996, **40**, 899-916.
24. B. J. Maranzano and N. J. Wagner, *Journal of Chemical Physics*, 2002, **117**, 10291-10302.
25. Y.-F. Lee, Y. Luo, T. Bai, C. Velez, S. C. Brown and N. J. Wagner, *Physics of Fluids*, 2021, **33**, 033316.
26. X. Cheng, J. H. McCoy, J. N. Israelachvili and I. Cohen, *Science*, 2011, **333**, 1276-1279.
27. J. R. Melrose and R. C. Ball, *Journal of Rheology*, 2004, **48**, 937-960.
28. N. J. Wagner and J. W. Bender, *Mrs Bulletin*, 2004, **29**, 100-106.
29. J. R. Melrose and R. C. Ball, *Journal of Rheology*, 2004, **48**, 961-978.
30. G. Batchelor and J. Green, *Journal of Fluid Mechanics*, 1972, **56**, 401-427.
31. G. Batchelor and J.-T. Green, *Journal of Fluid Mechanics*, 1972, **56**, 375-400.
32. J. Bergenholtz, J. F. Brady and M. Vivic, *Journal of Fluid Mechanics*, 2002, **456**, 239-275.
33. A. J. Banchio and J. F. Brady, *The Journal of chemical physics*, 2003, **118**, 10323-10332.
34. R. Mari, R. Seto, J. F. Morris and M. M. Denn, *Proc Natl Acad Sci U S A*, 2015, **112**, 15326-15330.
35. D. P. Kalman and N. J. Wagner, *Rheologica Acta*, 2009, **48**, 897-908.
36. G. Bogush, M. Tracy and C. Zukoski Iv, *Journal of non-crystalline solids*, 1988, **104**, 95-106.
37. C. d. de Kruif, E. Van Iersel, A. Vrij and W. Russel, *The Journal of chemical physics*, 1985, **83**, 4717-4725.
38. W. B. Russel, N. J. Wagner and J. Mewis, *Journal of Rheology*, 2013, **57**, 1555-1567.
39. J. Barker, C. Glinka, J. Moyer, M. Kim, A. Drews and M. Agamalian, *Journal of Applied Crystallography*, 2005, **38**, 1004-1011.
40. J. B. Hipp, J. J. Richards and N. J. Wagner, *Journal of Rheology*, 2019, **63**, 423-436.
41. L. Porcar, D. Pozzo, G. Langenbacher, J. Moyer and P. D. Butler, *Review of scientific Instruments*, 2011, **82**, 083902.
42. S. R. Kline, *Journal of applied crystallography*, 2006, **39**, 895-900.
43. F. Oosterhelt, M. Rief and H. Gaub, *New Journal of Physics*, 1999, **1**, 6.
44. L.-N. Krishnamurthy, N. J. Wagner and J. Mewis, *Journal of rheology*, 2005, **49**, 1347-1360.
45. B. M. Guy, M. Hermes and W. C. K. Poon, *Phys. Rev. Lett.*, 2015, **115**.

46. N. Fernandez, J. Cayer-Barrioz, L. Isa and N. D. Spencer, *Langmuir*, 2015, **31**, 8809-8817.
47. R. Seto and G. G. Giusteri, *Journal of Fluid Mechanics*, 2018, **857**, 200-215.
48. J. R. Royer, D. L. Blair and S. D. Hudson, *Phys Rev Lett*, 2016, **116**, 188301.
49. E. Brown and H. M. Jaeger, *Journal of Rheology*, 2012, **56**, 875-923.
50. E. Brown and H. M. Jaeger, *Rep Prog Phys*, 2014, **77**, 046602.
51. R. Maharjan, E. O'Reilly, T. Postiglione, N. Klimenko and E. Brown, *Phys. Rev. E*, 2021, **103**, 012603.
52. A. K. Gurnon, P. D. Godfrin, N. J. Wagner, A. P. Eberle, P. Butler and L. Porcar, *JoVE (Journal of Visualized Experiments)*, 2014, e51068.
53. S. Pradeep and L. C. Hsiao, *Soft Matter*, 2020, **16**, 4980-4989.
54. N. J. Wagner and B. J. Ackerson, *The Journal of Chemical Physics*, 1992, **97**, 1473-1483.
55. B. Saint-Michel, T. Gibaud and S. Manneville, *Physical Review X*, 2018, **8**, 031006.
56. J. E. Thomas, A. Goyal, D. Singh Bedi, A. Singh, E. Del Gado and B. Chakraborty, *Journal of Rheology*, 2020, **64**, 329-341.
57. J. E. Thomas, K. Ramola, A. Singh, R. Mari, J. F. Morris and B. Chakraborty, *Phys. Rev. Lett.*, 2018, **121**, 128002.